Structure and Electromagnetic Properties of $Bi_{1-x}Y_xFe_{0.95}Mn_{0.05}O_3$(x=0.05, 0.075 and 0.10)

J. Silva, A. Reyes, R. Castañeda, H. Esparza, H. Camacho, J. Matutes, and L. Fuentes

Abstract

The effect of Y and Mn co- doping on the structural and electromagnetic properties of $BiFeO_3$ is described. Multiferroic ceramics of $Bi_{1-x}Y_xFe_{0.95}Mn_{0.05}O_3$ (x = 0.05, 0.075 and 0.10) have been synthesized by the sol- gel method. Phase, structure and microstructure analyses were performed by scanning electron microscopy and X-ray diffraction followed by Rietveld analysis. Y saturation and consequent formation of a secondary phase was observed. Electric andmagneticmeasurements show that investigated doping is beneficial. Dielectric loses decreases, ferroelectric and ferromagnetic loops compare favorably with those corresponding with competing compositions.

Keywords: Doped $BiFeO_3$; electromagnetic properties; Rietveld strain detection.

Introduction

Magnetoelectric multiferroics exhibit ferroelectric and some kind of magnetic order simultaneously [1–4]. These materials motivate interest, mostly due to their potentialities in the field of non-volatile memories. The basic idea is to write data as electrically-driven magnetization [5]. Ferroelectricity in bismuth perovskites is provoked by eccentricity of the A (Bi) cation, while the magnetic B cation triggers magnetic ordering [6]. The most widely studied multiferroic is $BiFeO_3$ (BFO). It shows rhombohedral R3c symmetry, G-type antiferromagnetism with T_N ~370°C and ferroelectricity up to T_C ~830°C [7]. Frequently, this material is found to be

contaminated by $Bi_2Fe_4O_9$ and $Bi_{25}FeO_{40}$ that are formed during the synthesis process [8]. As described in detail in ref [9], several $BiFeO_3$ preparation methods have been proposed. Some representative techniques are the following: solid state [10], rapid sintering [11], mechanoactivation [12], hydrothermal [13], combustion [14], sonochemistry [15], molten salts [16] and sol-gel [17]. The sol-gel process is an excellent technique to explore compositional variants, because it allows stoichiometry control and favors the homogeneity of the resulting material. It also facilitates working at lower temperatures and controlling the particle size.

Doping the A-sitewith alkaline earth and rare earthmetals has been widely studied. Ba, Sr have been used to reduce grain size, improve resistivity, stabilize the pure rhombohedral phase and enhance magnetic ordering. Ferroelectric response, on the other hand, has been weakened [18–21]. Rare earths, mostly La, help preserving the purity of the rhombohedral phase and uphold the ferroelectric properties [22–24].

Specific reports on A-site doping with Y are limited and do not show coincidence regarding crystal structure. Feng et al. [25] report that R3c BFO is preserved up to 20% Y, but, starting at 5% Y, secondary $Y_3Fe_5O_{12}$ is formed. Bellakki and Manivannan [26] mention that 10% Y leads BFO to an orthorhombic-like symmetry tranformation. Mishra *et al*. [27] observe a change to tetragonal symmetry at 10% Y.

B-site doping is used to break the spin cycloid that characterizes antiferomagnetism in BFO (transition metals) [28–30] and to reduce leakage currents (Ti, Zr, Mn) [31–33].

To our knowledge, co-doping with Y and transition metals has not been described. In the present paper the effect of Y and Mn co-doping in $BiFeO_3$ ceramics, prepared by sol gel method, is reported.

Experimental

Four compositions, corresponding to formulas BiFeO3 and $Bi_{1-x}Y_xFe_{0.95}Mn_{0.05}O_3$ (x = 0.05, 0.075 and 0.10), were investigated. Samples were synthesized by sol-gel method. Stoichiometric amounts of $Bi(NO_3)_3{\cdot}5H_2O$, $Fe(NO_3)_3{\cdot}9H_2O$, $Y(NO_3)_3{\cdot}6H_2O$ and $Mn(NO_3)_2{\cdot}4H_2O$ were dissolved in a 1.5 N nitric acid solution. The molar ratio of metal/tartaric acid/ethylene glycol was 1/2/36. The solution was kept under stirring for two hours at a temperature of 70°C. Afterwards, it was allowed to dry. Drying was performed at 160°C for 2 hours. Carbonization was accomplished at 250°C for two hours, after a ramp of 2°C/min to prevent ignition. The powders were removed from the oven, grounded in an agate mortar and placed in an alumina crucible. Starting at 300°C and with a ramp of 5°C/min, the samples were taken to the calcination temperature of 600°C, where they remained for two hours.

Powder X-ray diffraction (XRD) experiments were performed in a PANalytical X'pertPRO diffractometer with CuKα radiation operated at 40 kV and 35 mA in the 2θ range of 20–60°. Rietveld analysis of XRD patterns was accomplished by use of Fullprof program [34].

Pellets were compacted under uniaxial pressure of 360 MPa and sintered in a temperature range 845°C < T < 860°C for three minutes and then cooled to room temperature.

The pellets were silver-painted on both sides. Impedance was measured by means of a HP4192A spectroscope. Ferroelectric hysteresis loops were determined by using a Radiant Technologies P-WS/Dsystem. Magnetic hysteresis loops were studied in a Quantum Design PPMS VSM with a maximum field of 25 KOe.

For microstructural investigation, the pellets were fractured and studied by scanning electron microscopy (SEM) on a JSM7401F equipment.

Results and discussion

Figure 1 shows the room temperature XRD patterns of investigated samples in powder form.

Pure $BiFeO_3$ produces its characteristic rhombohedral R3c diffraction pattern.

At first sight, the XRD diagrams of doped samples do not give clear evidence of departure from cubic symmetry. Characteristic R3c 006 peak is not unambiguously separated from intense R3c 202 maximum and R3c 113 peak (if present) lies in the detection limit.

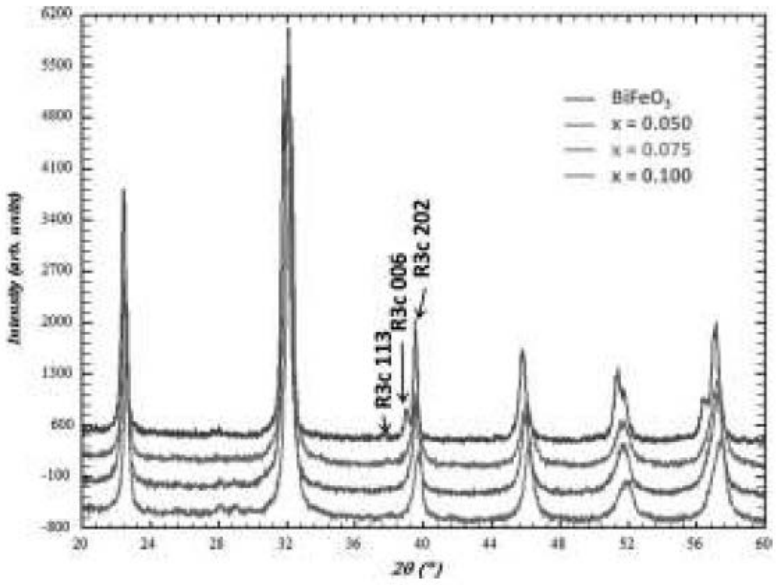

Figure 1. Powder XRD patterns of $BiFeO_3$ and $Bi_{1-x}Y_xFe_{0.95}Mn_{0.05}O_3$.

For the sample with x = 0.05, no impurity phases are observed. Antiferromagnetic orthorhombic $Bi_2Fe_4O_9$ precipitation starts at x = 0.075 (observe weak signals at 28° < 2θ < 30°) and, for x = 0.1, the presence of $YFeO_3$ is to be considered in the detection limit (very weak peak at 2θ ≈ 25°).

To stand on a quantitative basis the mentioned qualitative interpretation, Rietveld analysis was applied. Initial crystal structure data for BFO (space group, cell geometry and asymmetric unit) were taken from reference [35]. Attention was focused on phase analysis, lattice parameters variations and crystal perfection.

Figure 2 shows the Rietveld fitting of the x = 0.10 diffractogram (the most complex one). Table 1 summarizes the results of the Rietveld analyses performed to all the samples.

Regarding phase analysis, Rietveld refinement gives reasonable figures for $Bi_2Fe_4O_9$ concentrations in the x=0.075 and 0.10 samples.Asubsequent conclusion is that secondary phases are all in the range of 5% or below.

The determination of lattice parameters and crystal symmetry is correlated with peakbroadening phenomena. The two main causes of peak broadening are small crystal size (broadening ∝ cos θ) and heterogeneous strain (broadening ∝ tg θ). To clarify the relative contributions of the mentioned effects, Fullprof capability for investigating crystal perfection [36] was applied.

Fullprof was run with the commands for simultaneously fitting of hexagonal lattice parameters, small crystal size and micro-strains. Optimization of Rietveld agreement factors (X^2, R_{wp}) lead to the conclusion that peak broadening is due, principally, to

heterogeneous cell dimensions. Non-detectable crystal size contribution to peak broadening means that average crystallites are of the order of 100 nm or larger.

Results in Table 1 include lattice parameters according to hexagonal and rhombohedral coordinate systems. The tendency of cell dimensions to contract with increasing Y content is apparent. Ionic radii of Bi^{3+} and Y^{3+} are, respectively, 1.2 and 0.95 Å. In the lattice parameters columns, figures inside parenthesis, uncertainties in general, have different meanings for the pure $BiFeO_3$ row and for the doped cases.

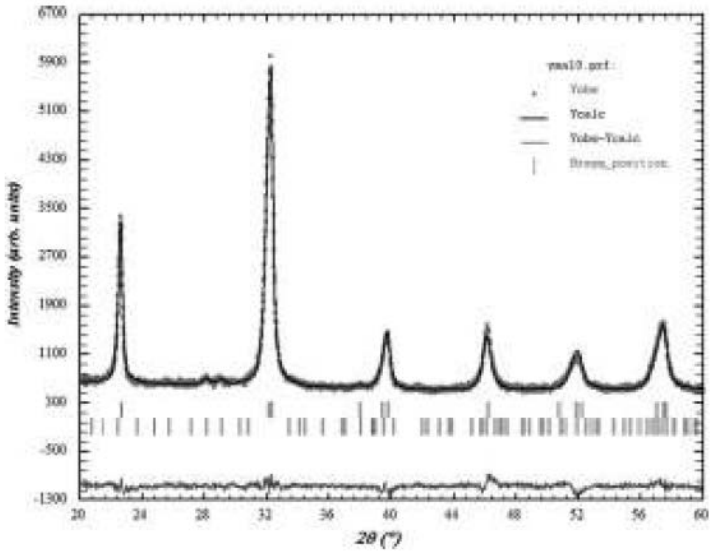

Figure 2. Rietveld analysis of sample $Bi_{90}Y_{0.10}Fe_{0.95}Mn_{0.05}O_3$. Agreement factors: $R_{wp} = 12.1$; $\chi^2 = 1.95$. Peaks' broadening, basically due to micro-strains, introduces ambiguity regarding doped BFO crystal symmetry. Secondary phase is antiferromagnetic $Bi_2Fe_4O_9$.

In the BFO refinement, uncertainties in lattice parameters are the standard deviations given by Fullprof. In doped samples, figures inside parenthesis were obtained by application of strain results to lattice parameters. The rhombohedral description of cell geometry is illustrative. Angle α = 60◦ means cubic cell geometry. BFO is clearly rhombohedral and doped samples show such variations in cell geometry that departure from cubic geometry cannot be resolved. The origin of cell parameters

variations can be found in non-homogeneity of the cations distribution. Comparison of present results with those of reference [26] may be opportune. Unfortunately, diffraction data interpretation in the considered article cannot be followed in detail, because Rietveld "y_{obs}–y_{calc}" plots are not shown.

Table 1
Selected Rietveld results. $BiFeO_3/Bi_{1-x}Y_xFe_{0.95}Mn_{0.05}O_3$

		BFO lattice parameters				
		Hexagonal system		Rhombohedral system		BFO Strain
Sample	% $Bi_2Fe_4O_9$	a(Å)	c(Å)	a(Å)	α(°)	(%)
$BiFeO_3$	0	5.5777(2)	13.859(1)	5.6313(1)	59.371(1)	—
$x = 0.050$	detection limit	5.57(5)	13.8(1)	5.60(5)	59.6(6)	90(10)
$x = 0.075$	2(1)	5.57(4)	13.8(1)	5.60(4)	59.6(5)	78(10)
$x = 0.100$	5(1)	5.55(4)	13.7(1)	5.59(4)	59.5(5)	80(10)

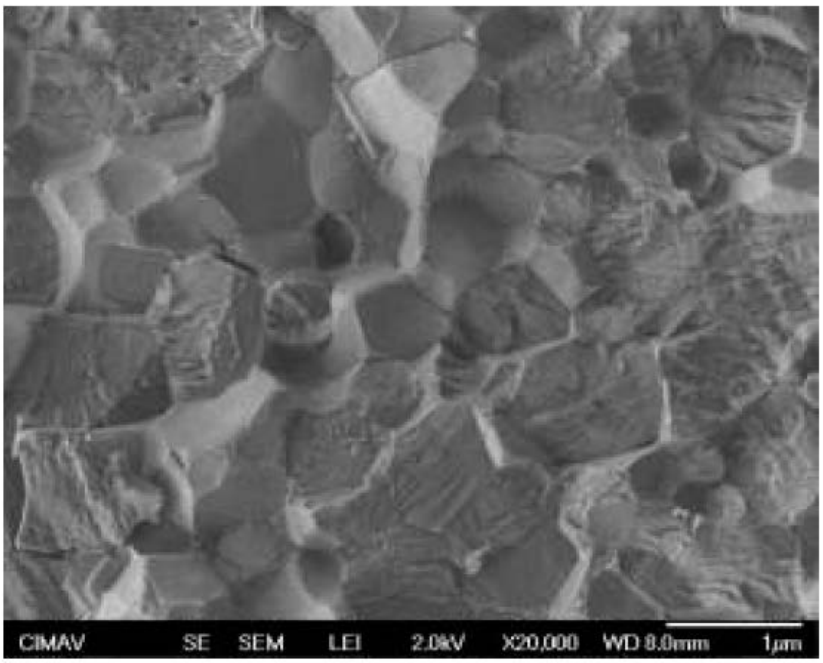

Figure 3. SEM image of fractured ceramic. $Bi_{0.95}Y_{0.05}Fe_{0.95}Mn_{0.05}O_3$.

Interesting diffraction signals, for example peak broadening/splitting at 2θ ≈ 46° for x = 0.10, do not fit with the rhombohedral structure reported in Table 1 of the mentioned article. If a user of the Inorganic Crystal Structure Database (ICSD) [37] reads the card # 168743 (based on reference [26]) and plots the associated XRD pattern, he (she) finds at 2θ ≈ 46° a single, sharp peak that does not correspond with the observed signal in the original paper.

Figures 3, 4 and 5 show respectively the SEM images of ceramics corresponding with the compositions x = 0.05, 0.075 and 0.10. Some features of samples microstructures deserve mention.

Grain size is about 1 μm for x = 0.05 and decreases with increasing doping down to some hundreds nm for x = 0.10. Possibly, particle growth is inhibited by the formation of secondary phases.

Grain surface irregularities, characteristic of stress-induced fractures, decrease significantly as Y content increases. The interpretation that is proposed for this tendency is as follows. For x = 0.05, Y doping generates stress due to a close-to-supersaturation condition of the solid solution. Upon higher doping, secondary phases' precipitation releases stresses and so the brittle fracture SEM images show flat crystal faces. This interpretation is consistent with XRD results.

Figure 6 shows the frequency responses of the dielectric constant and loss tangent. It is observed that these properties remain practically constant as yttrium content increases. The dielectric constant value is relatively high at lowfrequencies and it decreaseswith increasing frequency. This behavior has been reported previously and the majority of authors agree that it is due to the space charge relaxation [38, 39]. The

loss factor at high frequency is comparable to the one reported in [27] and better than that of [25]. Both these works use yttrium as a dopant.

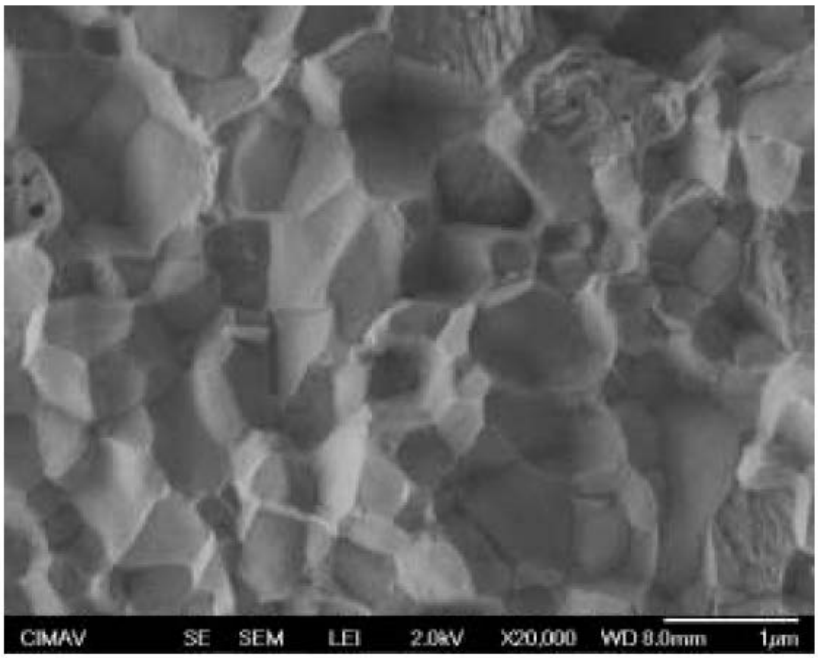

Figure 4. SEM image of fractured ceramic. $Bi_{0.925}Y_{0.075}Fe_{0.95}Mn_{0.05}O_3$.

Ferroelectric hysteresis loops were measured for different compositions. Figure 7 displays the results of measurements realized at 500 Hz. The obtained responses are typical for this class of materials, slightly better than the performances reported by [25, 27]. The increase of yttrium content does not affect ferroelectricity in a significative way.

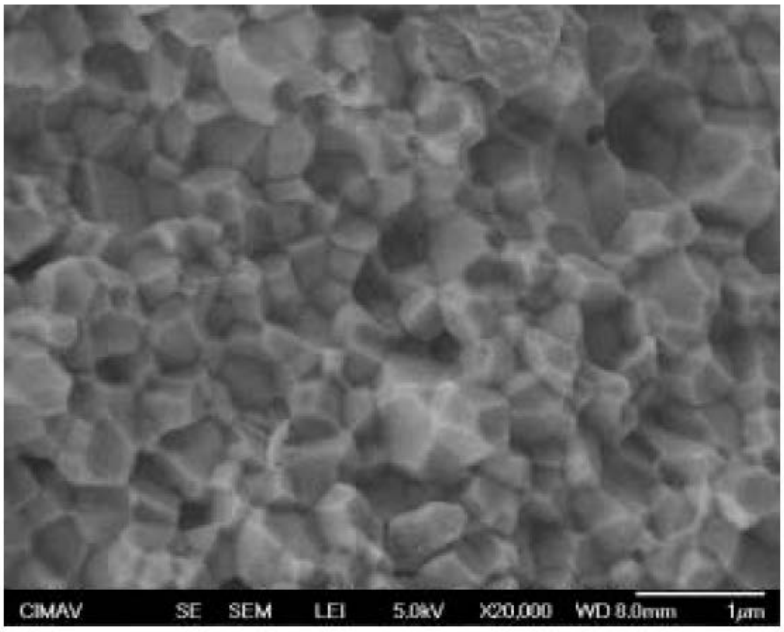

Figure 5. SEM image of fractured ceramic. $Bi_{0.90}Y_{0.10}Fe_{0.95}Mn_{0.05}O_3$.

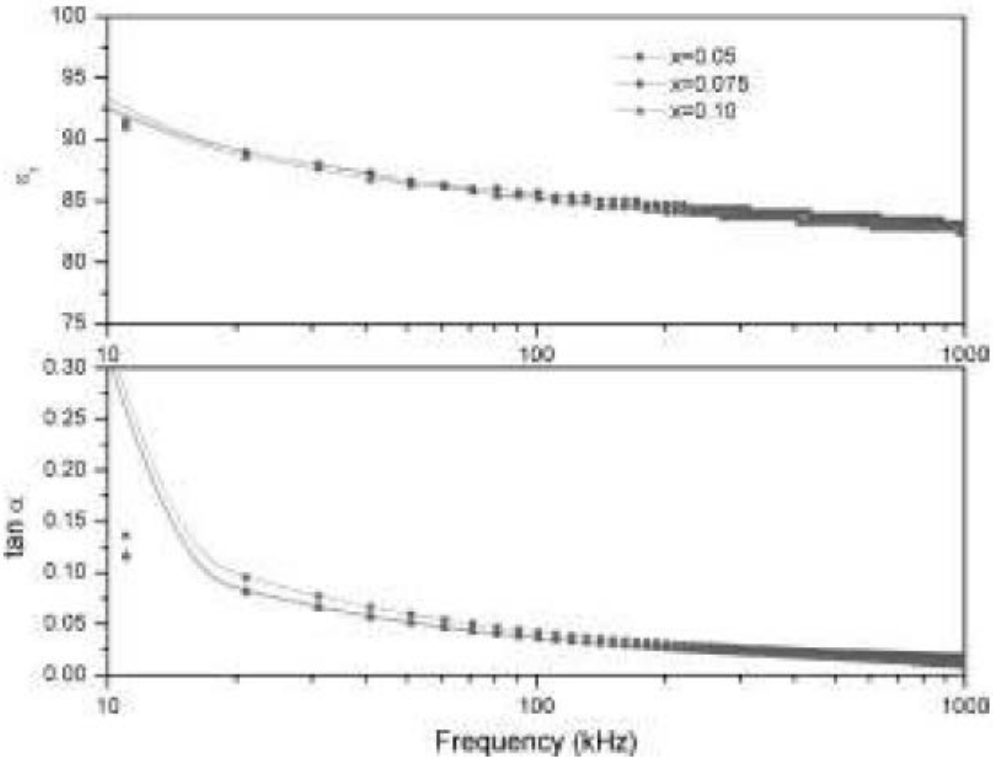

Figure 6. Dielectric constant and tangent loss $Bi_{1-x}Y_xFe_{0.95}Mn_{0.05}O_3$.

Figure 8 shows the magnetic hysteresis loops of the investigated materials under magnetic fields from 0 to 25 KOe at room temperature. Although magnetic order is observable, saturation magnetization is not reached under the conditions of the experiment. The remanent mangnetization increases with the Y content, assuming the values 0.017, 0.030 and 0.05 emu/gr for x = 0.050, 0.075 and 010 respectively. Presumably, magnetization is favored by the introduced dopants via destruction of the BFO characteristic spin cycloid. The observed secondary phase ($Bi_2Fe_4O_9$) has no effect due to its antiferromagnetic nature.

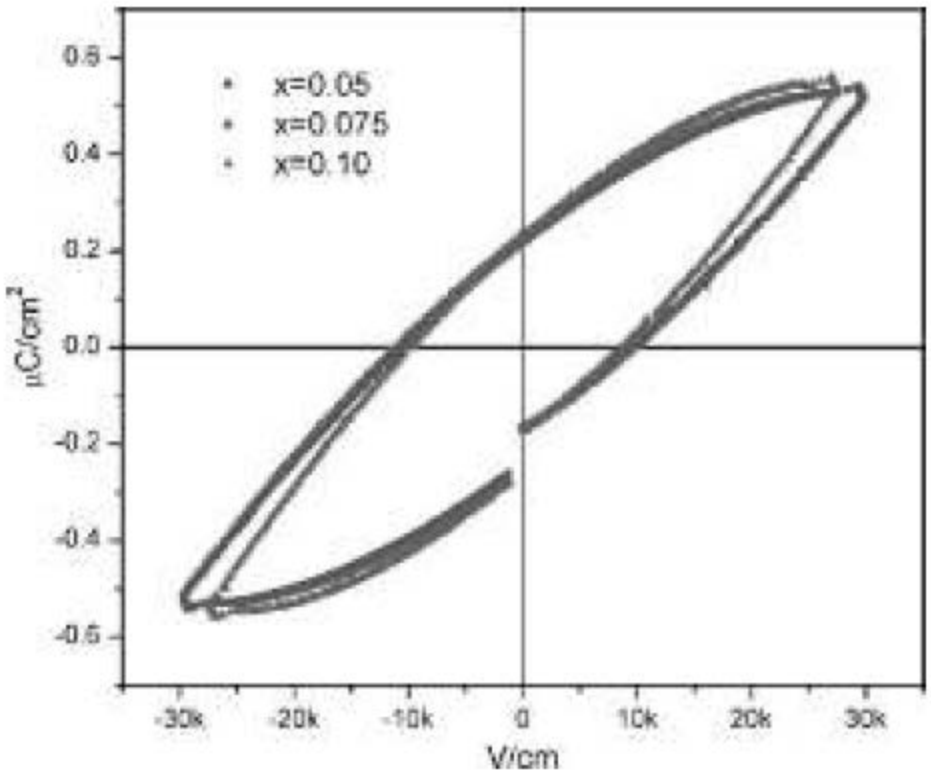

Figure 7. Ferroelectric hysteresis loops.of $Bi_{1-x}Y_xFe_{0.95}Mn_{0.05}O_3$ ceramics.

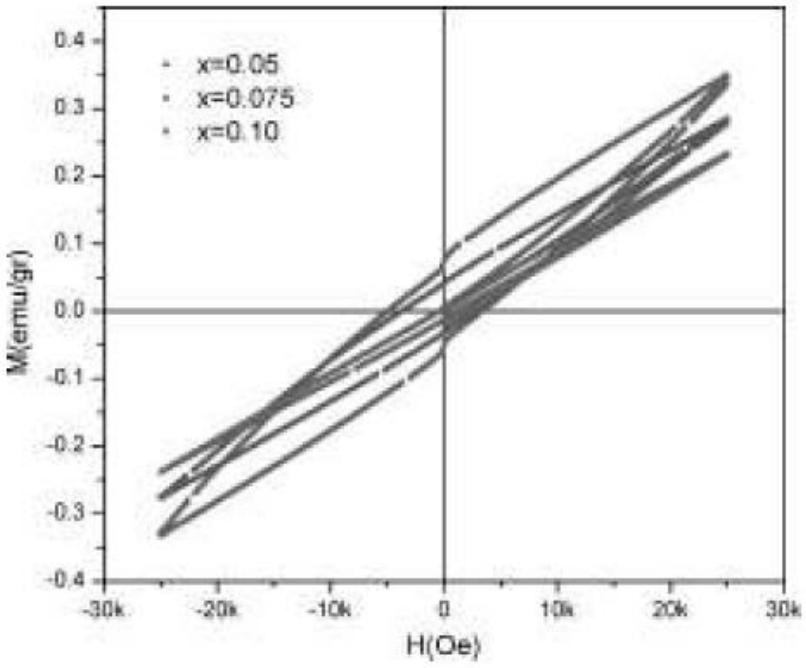

Figure 8. Magnetic hysteresis loops of $Bi_{1-x}Y_xFe_{0.95}Mn_{0.05}O_3$ ceramics at room. temperature.

Conclusions

Detailed investigation of the synthesis–structure–properties relationship in $Bi_{1-x}Y_xFe_{0.95}Mn_{0.05}O_3$ reveals the following: Single-phase solid solutions are obtained for $x < 0.075$. Minor secondary phases appear for higher content of Y. Rietveld analysis shows that significant microstrains, associated with chemical heterogeneities, are present.

Dielectric response is not substantially affected by an increase inYcontent. Acceptable ferroelectric hysteresis loops are obtained for all the considered compositions at 500 Hz.

Weak ferromagnetic responses appear, better defined with increased Y content, presumably as result of the collapse of the space modulated spin cycloidal structure.

Acknowledgments

Funding from Consejo Nacional de Ciencia y Tecnología, México (Projects CONACYT 102171 and 25380) is gratefully acknowledged. Present research has been also supported by Internal Projects of the Chemical Sciences Faculty, Autonomous University of Chihuahua. Thanks to M. Sc. Enrique Torres, M. Sc. Carlos Santillán and M. Sc. Daniel Lardizabal for continuous attention to the experimental work.

References

1. N. A. Hill, J. Phys. Chem B 104, 6694 (2000).

2. W. Erenstein, N. D. Mathur, and J. F. Scott, Nature 442, 759–765 (2006).

3. N. A. Spaldin and M. Fiebig, Science 309, 391 (2005).

4. L. E. Fuentes-Cobas, J. A. Matutes-Aquino, and M. E. Fuentes-Montero, Magnetoelectricity. Chapter 3 in K. H. J. Buschow, Editor, Handbook of magnetic materials, vol. 19, Elsevier (2011).

5. M. Bibes and A. Barthélémy, Nature Materials 7, 425–426 (2008).

6. N. A. Spaldin, Analogies and differences between Ferroelectrics and Ferromagnets. Physics of Ferroelectrics: A Modern Perspective. K.M. Rabe, C. H. Ahn, J. M. Triscone Editors. Book Series: Topics in Applied Physics 105, 175–217 (2007).

7. A. J. Jacobson and B. E. Fender, J. Phys. C. 8, 844 (1975).

8. M. Valant, A. K. Axelsson, and N. Alford, Chem. Mater. 19, 5431–5436 (2007).

9. J. Silva, A. Reyes, H. Esparza, H. Camacho, and L. Fuentes, Integrated Ferroelectrics 126, 47–59 (2011).

10. M. Mahesh Kumar, V. R. Palkar, K. Srinivas, and S. V. Suryanarayana, Appl. Phys. Lett. 76, 2764 (2000).

11. Y. P. Wang, L. Zhou, M. F. Zhang, X. Y. Chen, J.-M. Liu, and Z. G. Liu, Appl. Phys. Lett. 84, 1731 (2004).

12. D. Maurya, H. Thota, K. S. Nalwa, and A. Garg, J. Alloys Compd. 477, 780–784 (2009).

13. J. Prado-Gonjal, M. E. Villafuerte-Castrej´on, L. Fuentes, and E. Moran, Mater. Res. Bull. 44, 1734–1737 (2009).

14. S. Vijayanand, H. S. Potdar, and P. A. Joy, Appl. Phys. Lett. 94, 182507 (2009).

15. R. Mazumder, S. Ghosh, P. Mondal, D. Bhattacharya, S. Dasgupta, N. Das, A. Sen, K. Tyagi, M. Sivakumar, T. Takami, and H. Ikuta, J. Appl. Phys. 100, 033908 (2006).

16. J. Chen, R. Yu, L Li, C. Sun, T. Zhang, H. Chen, and X. Xing, Eur. J. Inorg. Chem. 23, 3655–3660 (2008).

17. S. M. Selbach, M. A. Einarsrud, T. Tybell, and T. Grande, J. Am. Ceram. Soc. 90, 3430–3434 (2007).

18. A. Gautam and V. S. Rangra, Cryst. Res. Technol. 45, 953–956 (2010).

19. D. H. Wang, W. C. Goh, M. Ning, and C. K. Ong, Appl. Phys. Lett. 88, 212907 (2006).

20. Ch. Yang, J. S. Jiang, F. Z Qian, D. M Jiang, Ch. M. Wang, and W. G. Zhang, J. Alloys Compd. 507, 29–32 (2010).

21. L. Y. Wang, D. H. Wang, H. B. Huang, Z. D. Han, Q. Q. Cao, B. X. Gu, and Y. W. Du, J. Alloys. Compd. 469, 1–3 (2009).

22. S. T. Zhang, L.H. Pang, Y. Zhang, M. H. Lu, and Y. F. Chen, J. Appl. Phys. 100, 114108 (2006).

23. G. L. Yuan, S.W. Or, and H. L. Chan, J. Phys. D 40, 1196–1200 (2007).

24. S. R. Das, R. N. P. Choudhary, P. Bhattacharya, R. S. Katiyar, P. Dutta, A. Manivannan, and M. S. Seehra, J. Appl. Phys. 101, 034104 (2007).

25. B. L. Feng, H. Xue, and Z. X. Xiong, Chinese Sci. Bull. 55, 452–456 (2010).

26. M. B. Bellakki and V. Manivannan, J. Sol-Gel Technol. 53, 184–102 (2010).

27. R. K. Mishra, D. K. Pradhan, R. N. P. Choudhary, and A. Banerjee, J. Phys.: Condens. Matter. 20, 045218 (2008).

28. F. Chang, N. Zhang, F. Yang, S. Wang, and G. Song, J. Phys. D 407799–7803 (2007).

29. Y. Wang, G. Xu, L. Yang, Z. Ren, X. Wei, W. Weng, P. Du, G. Shen, and G. Han, Mater. Lett. 62, 3806–3808 (2008).

30. Q. Xu, H. Zai, D. Wu, T. Qiu, and M. X. Xu, Appl. Phys. Lett. 95, 112510 (2009).

31. M. Kumar and K. L. Yadav, J. Appl. Phys. 100, 074111 (2006).

32. A. Ianculescu, F. Prihor, P. Postolache, O Oprea, and LMitoseriu, J. Alloys Compd. 504, 420–426 (2010).

33. K. Abe, N. Sakai, J. Takahashi, H. Itoh, N. Adachi, and T. Ota, Jpn. J. Appl. Phys. 49(9): 09MB01-6 (2010).

34. J. Rodr´ıguez-Carvajal, Physica B. 192, 55–69 (1993).

35. A. Reyes, C. de la Vega,M. E. Fuentes, and L. Fuentes, Journal of the European Ceramic Society 27, 3709–3711 (2007).

36. L. Fuentes, Synchrotron Radiation Diffraction and Scattering in Ferroelectrics. Chapter 6 in L. Pardo, J. Ricote Editors. Multifunctional Polycrystalline FerroelectricMaterials, Springer-Verlag (2011).

37. Inorganic Crystal Structure Database. http://www.fiz-karlsruhe.de/icsd.html

38. X. Zhang, Y. Sui, X. Wang, Y. Wang, and Z. Wang, J. Alloys Compd. 507, 157–161 (2010).

39. P. Uniyal and K.L. Yadav, J. Phys. Condens. Matter 21, 012205 (2009).

40. S. Zhang, W. Luo, D. Wang, and Y. Ma, Mater. Lett. 63, 1820–1822 (2009).